Radiological Physics and Technology (2019) 12:351–356
https://doi.org/10.1007/s12194-019-00527-5

Evaluation of a 3D-printed heterogeneous anthropomorphic head and neck phantom for patient-specific quality assurance in intensity-modulated radiation therapy

Noriyuki Kadoya[1] · Kota Abe[1,2] · Hikaru Nemoto[1] · Kiyokazu Sato[3] · Yoshiro Ieko[1,4] · Kengo Ito[1] · Suguru Dobashi[5] · Ken Takeda[5] · Keiichi Jingu[1]

Received: 2 March 2019 / Revised: 21 July 2019 / Accepted: 22 July 2019 / Published online: 30 July 2019

Abstract
We evaluated an anthropomorphic head and neck phantom with tissue heterogeneity, produced using a personal 3D printer, with quality assurance (QA), specific to patients undergoing intensity-modulated radiation therapy (IMRT). Using semi-automatic segmentation, 3D models of bone, soft tissue, and an air-filled cavity were created based on computed tomography (CT) images from patients with head and neck cancer treated with IMRT. For the 3D printer settings, polylactide was used for soft tissue with 100% infill. Bone was reproduced by pouring plaster into the cavity created by the 3D printer. The average CT values for soft tissue and bone were 13.0 ± 144.3 HU and 439.5 ± 137.0 HU, respectively, for the phantom and 12.1 ± 124.5 HU and 771.5 ± 405.3 HU, respectively, for the patient. The gamma passing rate (3%/3 mm) was 96.1% for a nine-field IMRT plan. Thus, this phantom may be used instead of a standard shape phantom for patient-specific QA in IMRT.

Keywords Radiotherapy · Quality assurance · Phantom · Structured exercise · 3D printer · Head and neck

1 Introduction

High conformal radiotherapy techniques, such as intensity-modulated radiation therapy (IMRT) and volumetric arc therapy, provide complex dose distributions with a sharp gradient; therefore, patient-specific quality assurance (QA) is necessary. Gamma index evaluation with a standard shape phantom has become the standard technique to compare measured and calculated distributions using a commercial radiation treatment planning system (TPS) [1]. Typically, for an acceptance criterion of 95% of points above a dose threshold, the gamma index should be < 1 for dose difference and distance-to-agreement limits of 3% and 3 mm, respectively [2, 3]. A previous study demonstrated the lack of correlation between conventional IMRT QA methods and dose errors in anatomical regions of interest [4]. Furthermore, Zhen et al. [5] reported a weak correlation between the gamma passing rate and critical patient dose volume histogram (DVH) errors. These previous findings demonstrate that gamma evaluation methods using existing phantoms may not accurately predict clinically relevant patient dose errors [5].

To solve this problem, an anthropomorphic patient-specific phantom has been developed [6]. The dose distribution of this anthropomorphic phantom is ideally equal to that of a patient undergoing computed tomography (CT). This phantom enabled us to adopt patient DVH-based QA instead of the gamma evaluation method using a standard shape phantom.

Recently, 3D printing has been used in the field of radiotherapy, and several 3D-printed materials (e.g., boluses) have already been used in clinical practice [7–17]. This

✉ Noriyuki Kadoya
kadoya.n@rad.med.tohoku.ac.jp

[1] Department of Radiation Oncology, Tohoku University Graduate School of Medicine, 1-1 Seiryo-machi, Aoba-ku, Sendai, Miyagi 980-8574, Japan

[2] Department of Radiation Oncology, Tokyo Metropolitan Cancer and Infectious Diseases Center Komagome Hospital, Tokyo 113-8677, Japan

[3] Department of Radiology, Tohoku University Hospital, Sendai, Miyagi 980-8574, Japan

[4] Department of Radiation Oncology, Yamagata University Faculty of Medicine, Yamagata, Japan

[5] Department of Radiological Technology, School of Health Sciences, Faculty of Medicine, Tohoku University, Miyagi 980-8574, Japan

3D printing technique could also be used to create an anthropomorphic phantom [6, 15, 16, 18]. If a personal 3D printer could be used to create this phantom, medical physicists would be able to easily create a similar phantom in hospitals. Ehler et al. [6] evaluated the feasibility of creating an anthropomorphic phantom using a personal 3D printer, using acrylonitrile butadiene styrene (ABS) as the printing material. However, because of the excessive heat required to extrude ABS plastic, the phantom could not be printed as a 100% solid object because of unacceptable deformation of the plastic on cooling. Instead, they printed the exterior shape of the phantom and filled it with a uniform mixture of a modified M3 mix. Kamomae et al. and Yea et al. also evaluated the feasibility of the 3D-printed anthropomorphic patient-specific head phantom [15, 16]. In these previous studies, the authors did not recreate the bone region (i.e., they recreated only the soft tissue and cavity regions). A 3D-printed anthropomorphic head phantom has been released as a commercial product (PseudoPatient™; RTsafe, San Antonio, TX, USA). This product can recreate the bone region, but there was no paper about detailed information of this phantom. In addition, evaluation of the geometric reproducibility of the 3D-printed phantom has been minimal.

Thus, we evaluated the feasibility of an anthropomorphic head and neck phantom with tissue heterogeneity created using a 3D printer.

2 Materials and methods

2.1 The 3D-printed head and neck phantom

We used planning CT images of a patient with head and neck cancer treated with IMRT in this study. This study was a retrospective analysis approved by our intuitional review board (2016-1-864). The workflow of creating the 3D-printed patient-specific head and neck phantom is shown in Fig. 1. First, the planning CT images were imported into in-house software based on Metasequoia 3D modeling software (Tetraface Inc., Tokyo, Japan). We modified the commercial 3D modeling software to perform the following steps using the graphical user interface. First, a 3D model reproducing three parts of the patient (bone, soft tissue, and air cavity) was created using semi-automatic segmentation. Regarding segmentations, the Otsu threshold method of discriminant analysis was used to segment the patient's body surface [19]. In addition, a threshold value of − 500 HU was used for the soft tissue (− 500 HU ≤ soft tissue region) and 200 HU for the bone (200 HU ≤ bone region). After automatic segmentation based on these criteria, each region was manually modified by an experienced medical physicist, particularly for regions with metal artifacts. A 3-cm-thick 3D model of the patient was then created. For pouring the liquid plaster into the cavity, we made thin walls (2-mm thick) at the inferior and superior ends of the phantom. Next, the 3D model that was exported to a standard triangulated language format was imported into Slicer software version 3.1.1

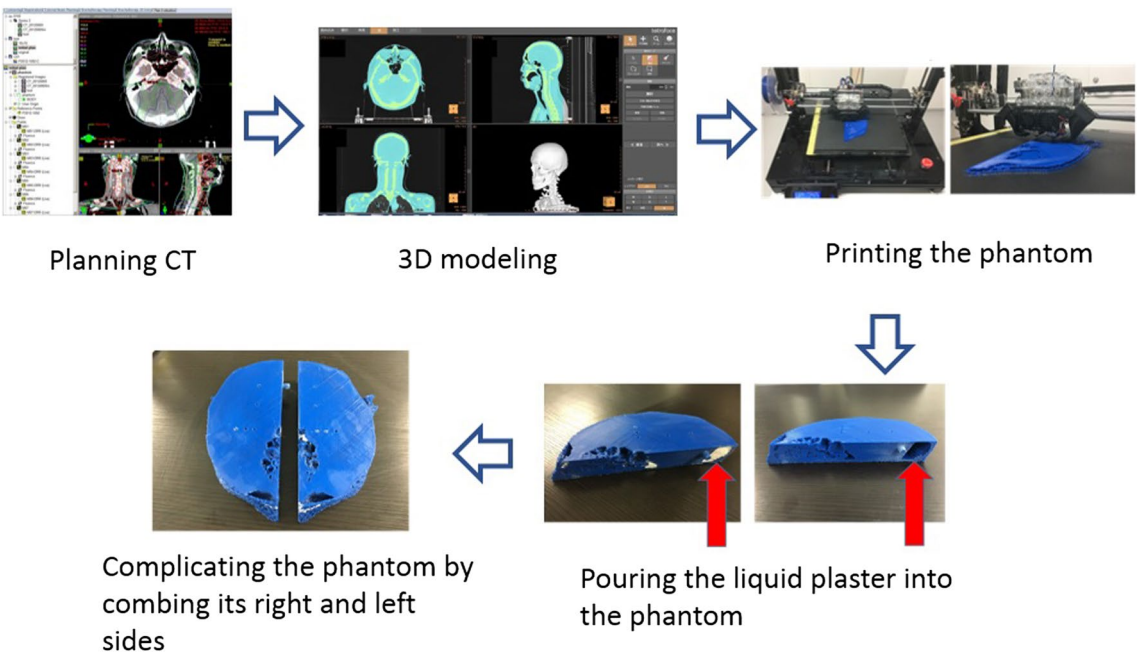

Fig. 1 Workflow for creating a 3D-printed patient-specific head and neck phantom

(Simplify3D, Cincinnati, OH, USA) to print the phantom using a 3D printer. The 3D printing was performed using fused deposition modeling on a Ninjabot NJB-300 W (Ninjabot, Shizuoka, Japan). Polylactide (PLA; Polymaker, Great Neck, NY, USA) was used as the 3D printing material for soft tissue with 100% infill. In a preliminary study, several materials were evaluated and found to be suitable for soft tissue (e.g., ABS or polycarbonate). Based on this preliminary study, PLA was selected as the material for the soft tissue, largely because of its reasonable CT value. The extraction temperature was 210 °C, layer height was 0.4 mm, and print speed (extrusion) was 20 mm/s.

Bone was subsequently reproduced by pouring plaster into the cavity of the phantom. First, to accurately pour the plaster into the entire cavity in the phantom created by the 3D printer, liquid plaster was prepared by mixing plaster powder (high-grade work plaster; Kateikagakukogyo Co.,Ltd., Osaka, Japan) and water at a ratio of 2:1. The physical density of the plaster was approximately 2.3 g/cm^3. The phantom was divided into two separate parts (right and left sides) into which the liquid plaster was poured to fill the entire cavity. The mixture then hardened.

2.2 CT image acquisition and treatment planning

All CT images were obtained using a LightSpeed RT16 system (GE Medical Systems, Brookfield, WI, USA). The settings for CT acquisition were 120 kV, 400 mA, and 0.5 s/rotation; slice thickness was 2.5 mm.

The TPS used in this study was Eclipse version 11.0 (Varian Medical Systems, Palo Alto, CA, USA). The Acuros XB dose calculation algorithm (dose-to-medium setting) implemented in Eclipse was selected for dose calculation because it provides accuracy comparable to the Monte Carlo method [20]. A treatment plan was created using eight-field IMRT; photon energy was 6 MV with gantry angles of 60°, 100°, 135°, 165°, 195°, 225°, 260°, and 300°. The prescription dose was 50 Gy, delivered in 25 fractions.

2.3 Evaluation of the physical characteristics of the phantom

To confirm the effectiveness of the phantom, the similarity of physical characteristics such as CT number and anatomical shape compared with the patient's CT image was evaluated. In terms of CT values, average CT values for soft tissue and bone, as well as the line profiles of CT values, were compared between the phantom and patient. In terms of anatomical shape, Dice similarity coefficients (DSCs) of CT images for surface, soft tissue, and bone were compared between the phantom and patient. DSC is often used to evaluate auto-segmentation accuracy and represents the volume overlap between two contours [21, 22]. For analysis of CT values and anatomical shapes, we used the contours of the body surface, soft tissue, and bone regions in all planes of the CT images.

As mentioned in Sect. 2.1, contours of the body surface, soft tissue, and bone in the patient's CT image were created using semi-automatic segmentation with manual modification by the medical physicist. In the same manner, we created the contours of the body surface, soft tissue, and bone in the phantom's CT. The average CT values and DSCs were calculated using two contours in the patient's and phantom's CT images. When the DSC is 1.0, the two contours matched perfectly. That is, the phantom could reproduce the anatomical shape accurately.

2.4 Evaluation of dose distribution of the phantom CT image

For dose comparison, we recalculated the dose distribution on a phantom CT image. First, automatic rigid registration using mutual information was performed between the phantom's and patient's CT images. Next, the dose distribution of the phantom CT image was recalculated using the same beam geometry and number of monitor units as in the patient's CT plan. Gamma analysis (3%/3 mm) was performed on the dose distributions calculated for the CT images of the phantom and patient.

3 Results

Figure 2 shows images of the newly created physical phantom, and Fig. 3 shows representative axial CT images of the phantom and patient. On visual inspection, the phantom CT image was considerably similar to that of the patient. However, there were differences around the nose and paranasal sinus between the two CT images. It should be noted that since there are 2-mm-thick walls on the inferior and superior ends of the phantom, we cannot see the internal structures in Fig. 2.

Table 1 shows the average CT values of soft tissue and bone in the phantom, showing reasonable agreement between the phantom and patient, particularly for soft tissue. In addition, Table 1 shows the DSCs for soft tissue, bone, and body surface. Although bone showed moderate agreement, the other two structures showed relatively good agreement between the phantom and patient. Figure 3 also shows two line profiles of CT values from both the phantom's and patient's CT images. In the soft tissue region, there was relatively good agreement between the phantom's and patient's CT line profiles. In contrast, in the bone region, slight differences in CT values were observed between the two profiles (maximum difference = 734.8 HU).

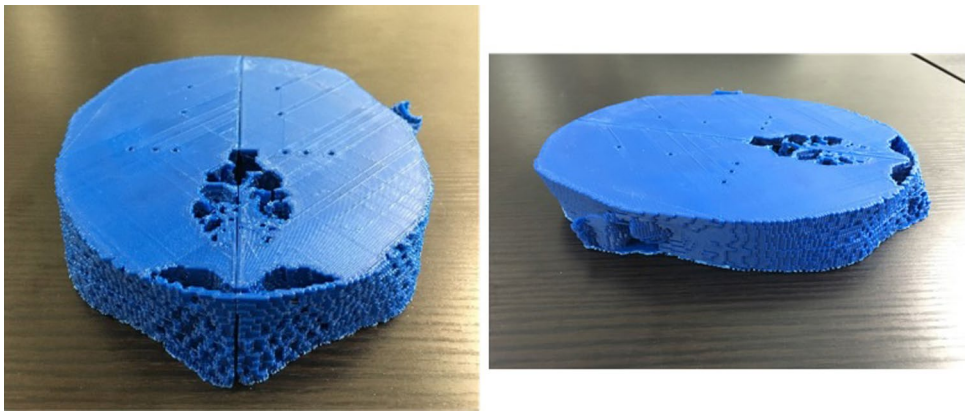

Fig. 2 Images of the newly created physical phantom

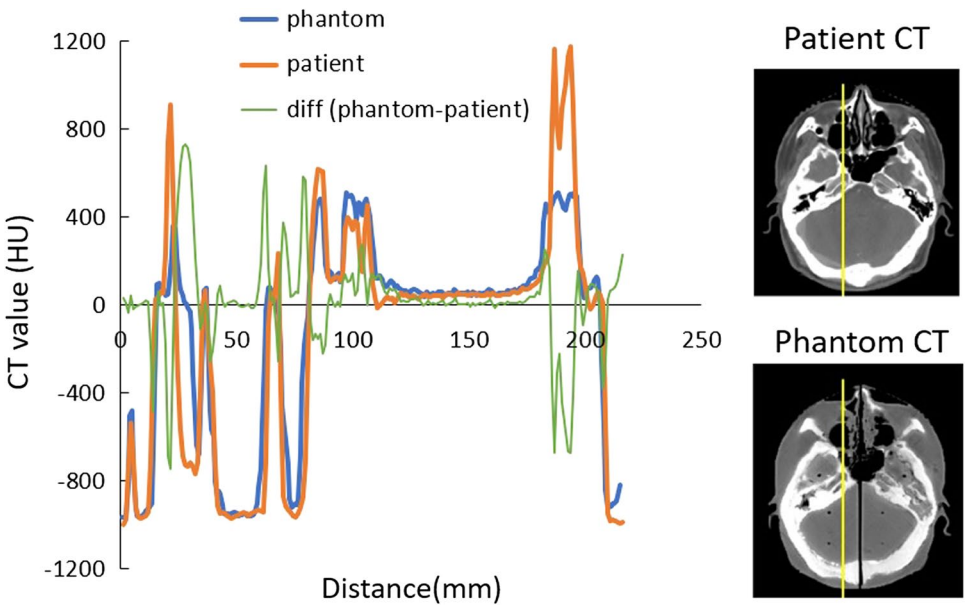

Fig. 3 Representative axial computed tomography images of the phantom and patient

Table 1 Summary of the average CT values and Dice similarity coefficients for each region

	Average CT value (HU)		DSC
	Patient	Phantom	
Soft tissue	12.1±124.5	13.0±144.3	0.81
Bone	771.5±405.3	439.5±137.0	0.71
Patient surface	–	–	0.92

DSC Dice similarity coefficient

Figure 4 shows the dose distributions of the phantom's and patient's CT images and the gamma analysis results (criteria: 3%/3 mm). The gamma passing rate for all areas in the 3D-printed phantom was 96.1%, showing good agreement between the two distributions. It should be noted that there were large dose differences between the two dose distributions near the body surface and bony regions.

4 Discussion

Ehler et al. [6] previously described the potential of 3D-printed head and neck phantoms. However, they could not reproduce soft tissue and bone using their 3D printing material, whereas our phantom could accurately reproduce the heterogeneity of different patient structures. They reported that the gamma passing rate (tolerance: 3%/3 mm) using films was 87.0% for superior axial images. In our data, the gamma passing rate without film dosimetry was 96.1% at almost the same slice as that described by Ehler et al. We calculated the gamma passing rate using two dose distributions calculated using the TPS, whereas Ehler et al. used two dose distributions measured using films. Consequently, their results included measurement uncertainty [6]. Their gamma passing rates differed from ours, possibly because their phantom did not reproduce the bone region. Kamomae et al. made a similar 3D-printed

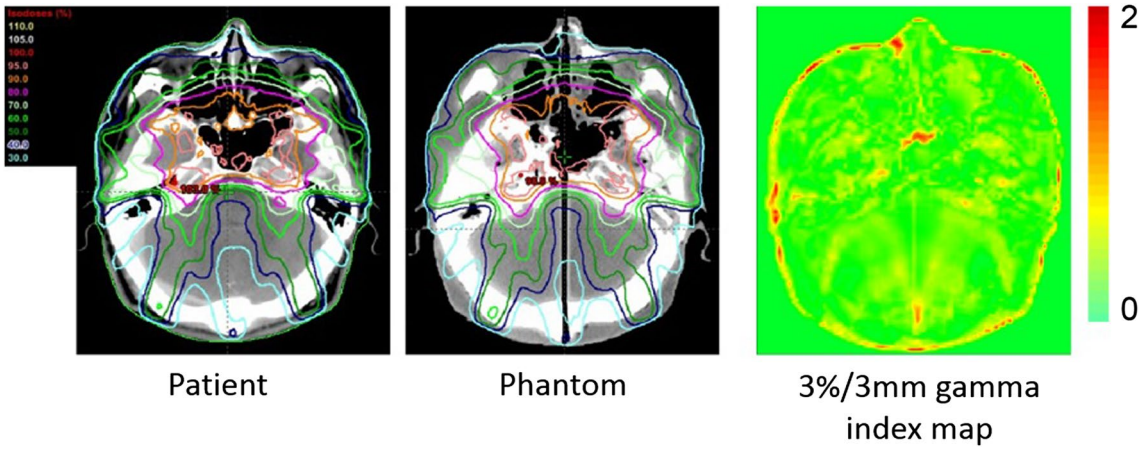

Fig. 4 Dose distributions of phantom and patient computed tomography images and a gamma index map (criteria: 3%/3 mm) obtained using an eight-field intensity-modulated radiation therapy plan

patient-specific phantom using the same material in the 3D printer (i.e., PLA) [15]. The average CT value of the soft tissue region was 12.7 HU, which is consistent with our result (12.1 HU). Because they did not reproduce the bone region, they had a relatively large difference in CT value around the bone region. The maximum difference was more than 1000 HU. On the other hand, in our study, the maximum difference was 734.8 HU. Based on this result, our phantom had the potential for improving the 3D-printed patient-specific phantom-based QA.

In terms of reproduction accuracy, the DSC of the bone region of our phantom was smaller than that of other structures because the liquid plaster may not have reached this region because of its complex structure. Using more liquid plaster may solve this issue; however, this may result in smaller CT values because of the increased water content. In future, we need to identify a reasonable ratio of plaster powder to water for this phantom. In addition, as shown in Fig. 3, there were anatomical differences around the nose and paranasal sinus between the CT images of the patient and phantom. The reason for this might be leaking of the liquid plaster. The extremely thin wall around the cavity may have caused the liquid plaster to leak, resulting in the different anatomical shapes in some regions.

It is ideal to perform patient-specific QA for patients undergoing IMRT by comparing the TPS dose on the patient's CT image and the measured dose using the 3D-printed patient-specific anthropomorphic head and neck phantom. Although our results showed reasonable agreement between patient and phantom in geometric and dosimetric accuracy, there were residual errors in accuracy for CT number and geometric reproducibility. To routinely use these 3D-printed phantoms in the clinic, further improvement is needed. Our study had a limitation in that we made only one 3-cm-thick phantom (i.e., not a whole phantom). Because of limited research funding, we could not create a whole phantom using the 3D printer. Although our phantom was only 3-cm thick, we believed that we could test the feasibility of our 3D-printed phantom to a certain extent. In the future, we will conduct a detailed evaluation using 3D-printed whole phantoms with more patient data.

5 Conclusions

We developed a novel 3D-printed anthropomorphic head and neck phantom that had CT values and dose distribution that were considerably similar to those of patient data. Consequently, this phantom could be used for patient-specific QA for IMRT instead of a standard shape phantom.

Funding This study was supported in part by the Japan Society for the Promotion of Science Grant-in-Aid for Young Scientists (B) (15K19199).

Compliance with ethical standards

Conflict of interest All authors have no conflicts of interest.

Ethical approval This article does not contain any studies with animals performed by any of the authors. All procedures performed in studies involving human participants were in accordance with the ethical standards of the institutional and/or national research committee and with the 1964 Declaration of Helsinki and its later amendments or comparable ethical standards. Informed consent was obtained from all individual participants included in the study.

References

1. Low DA, Harms WB, Mutic S, et al. A technique for the quantitative evaluation of dose distributions. Med Phys. 1998;25:656–61.

2. Ezzell GA, Burmeister JW, Dogan N, et al. IMRT commissioning: multiple institution planning and dosimetry comparisons, a report from AAPM task group 119. Med Phys. 2009;36:5359–73.
3. Masi L, Casamassima F, Doro R, et al. Quality assurance of volumetric modulated arc therapy: evaluation and comparison of different dosimetric systems. Med Phys. 2011;38:612–21.
4. Kruse JJ. On the insensitivity of single field planar dosimetry to IMRT inaccuracies. Med Phys. 2010;37:2516–24.
5. Zhen H, Nelms BE, Tome WA. Moving from gamma passing rates to patient DVH-based QA metrics in pretreatment dose QA. Med Phys. 2011;38:5477–89.
6. Ehler ED, Barney BM, Higgins PD, et al. Patient specific 3D printed phantom for IMRT quality assurance. Phys Med Biol. 2014;59:5763–73.
7. Mayer R, Liacouras P, Thomas A, et al. 3D printer generated thorax phantom with mobile tumor for radiation dosimetry. Rev Sci Instrum. 2015;86:074301.
8. Jung J, Song SY, Yoon SM, et al. Verification of accuracy of cyberknife tumor-tracking radiation therapy using patient-specific lung phantoms. Int J Radiat Oncol Biol Phys. 2015;92:745–53.
9. Burleson S, Baker J, Hsia AT, et al. Use of 3D printers to create a patient-specific 3D bolus for external beam therapy. J Appl Clin Med Phys. 2015;16:5247.
10. Madamesila J, McGeachy P, Villarreal Barajas JE, et al. Characterizing 3D printing in the fabrication of variable density phantoms for quality assurance of radiotherapy. Phys Med. 2016;32:242–7.
11. Arimura T, Ogino T, Yoshiura T, et al. A feasibility study of a hybrid breast-immobilization system for early breast cancer in proton beam therapy. Med Phys. 2017;44:1268–74.
12. Lukowiak M, Jezierska K, Boehlke M, et al. Utilization of a 3D printer to fabricate boluses used for electron therapy of skin lesions of the eye canthi. J Appl Clin Med Phys. 2017;18:76–81.
13. Zhao Y, Moran K, Yewondwossen M, et al. Clinical applications of 3-dimensional printing in radiation therapy. Med Dosim. 2017;42:150–5.
14. Filippou V, Tsoumpas C. Recent advances on the development of phantoms using 3D printing for imaging with CT, MRI, PET, SPECT, and ultrasound. Med Phys. 2018. https://doi.org/10.1002/mp.13058.
15. Kamomae T, Shimizu H, Nakaya T, et al. Three-dimensional printer-generated patient-specific phantom for artificial in vivo dosimetry in radiotherapy quality assurance. Phys Med. 2017;44:205–11.
16. Yea JW, Park JW, Kim SK, et al. Feasibility of a 3D-printed anthropomorphic patient-specific head phantom for patient-specific quality assurance of intensity-modulated radiotherapy. PLoS One. 2017;12:e0181560.
17. Kitamori H, Sumida I, Tsujimoto T, et al. Evaluation of mouthpiece fixation devices for head and neck radiotherapy patients fabricated in PolyJet photopolymer by a 3D printer. Phys Med. 2019;58:90–8.
18. Alqahtani MS, Lees JE, Bugby SL, et al. Design and implementation of a prototype head and neck phantom for the performance evaluation of gamma imaging systems. EJNMMI Phys. 2017;4:19.
19. Otsu N. A threshold selection method from gray-level histgrams. IEEE Trans Syst Man Cybern. 1979;9:6.
20. Tsuruta Y, Nakata M, Nakamura M, et al. Dosimetric comparison of Acuros XB, AAA, and XVMC in stereotactic body radiotherapy for lung cancer. Med Phys. 2014;41:081715.
21. Kadoya N, Miyasaka Y, Nakajima Y, et al. Evaluation of deformable image registration between external beam radiotherapy and HDR brachytherapy for cervical cancer with a 3D-printed deformable pelvis phantom. Med Phys. 2017;44:1445–55.
22. Dice LR. Measures of the amount of ecologic association between species. Ecology. 1945;26:297–302.